Two Dimensional Oxygen-deficient Bismuth oxy-iodide Nanosheets with Enhanced Supercapacitor Performances

Huichao Wang[1], Zhengde Wang [1], huadong Tian[1], Rongrong Cheng[1], Mohan Lin[1],
Xueqin Sun[2], Songlin Ran[3], Yaohui Lv[1,3,4,]*

[1] School of Materials Science and Engineering, Anhui University of Technology, Anhui, Maanshan, 243002, China.
[2] School of Environment and Material Engineering, Yantai University, Shandong, Yantai,264005, China.
[3] Key Laboratory of Green Fabrication and Surface Technology of Advanced Metal Materials (Anhui University of Technology), Ministry of Education, Maanshan, 243002, China
[4] Key Laboratory of Metallurgical Emission Reduction & Resources Recycling, Ministry of Education, Anhui University of Technology, Anhui, Maanshan, 243002, China.
[*]E-mail: yaohui@ahut.edu.cn

Introducing oxygen vacancy into oxides has become an effective strategy for enhancing the electrochemical performance. Herein, a series of identical two-dimensional BiOI nanosheets with various concentration of oxygen vacancies are rationally fabricated through a facile ion-exchange and annealing process under Ar atmosphere. The presence of oxygen vacancies has been identified by X-ray photoelectron spectroscopy (XPS) and high-resolution transmission electron microscopy (HRTEM). The X-ray diffraction (XRD) and field emission scanning electron microscopy (FESEM) are used to probe the evolution of crystal structure and morphology of the product. Electrochemical data show that reduced two-dimensional BiOI nanosheets electrodes with appropriate oxygen vacancies exhibit a significant improvement on capacitance compared to the pristine electrodes. The specific capacitance of the as-prepared BiOI-600 electrode reaches 620 F g^{-1} (at 0.5 A g^{-1}), and 65 % capacitance retention after 1000 cycles at 2 A g^{-1}. The good electrochemical performances can be mainly ascribed to the convenient diffusion of electrolyte ions (*e.g.* two dimensional nanosheets) and more surface active sites (*e.g.* oxygen vacancies) for redox reactions. These findings provide new chance for the oxygen-vacancies-rich two-dimensional BiOI nanosheets as high-performance supercapacitor electrodes.

Keywords: BiOI nanosheet, oxygen vacancy, supercapacitor, electrochemical energy storage

1. INTRODUCTION

Renewable energy and energy storage have long been the pursued objectives, with many efforts devoted to development of high-performance energy storage and conversion devices [1, 2]. In recent

years, supercapacitors (SCs) as one of the most favorable candidates for the energy storage devices, has drawn enormous research recognition due to their high power density, wide operating temperature range, fast charging and discharging rate and long cycle life [3]. According to the difference of the charge-storage mechanism, SCs can be classified into two categories, including electric double-layer capacitors (EDLCs) and pseudocapacitors. For EDLCs, carbon-based materials are commonly selected as electrodes owing to their good electrical conductivity and excellent chemical stability. However, carbon materials as SCs electrode feature low capacitance and energy density, limiting its further practical application [4]. On the contrary, electrode materials based on transition metal oxide (RuO_2 [5], MnO_2 [6], $NiCo_2O_4$ [7]) can exhibit higher specific capacitances through surface faradaic redox reaction. Nevertheless, the poor intrinsic electrical conductivity of transition metal oxide can induce the loss of the capacitance, exhibiting poor rate performance [8]. There are two major strategies to enhance their electrochemical performance. The first approach is to obtain 2D nanosheets with planar geometry for easy transport and migration of ions/electron [9]. Kim SJ [10] prepared siloxene sheets with high specific capacitance (2.18 F cm^{-2}) and energy density (9.82 mJ cm^{-2}). The second method is to introduce oxygen vacancy on the surface of the metal oxide material [11, 12]. In addition, theoretical studies illustrate that introducing surface oxygen vacancies in the metal oxide materials offer a new route to improve the the specific capacitance [13, 14].

Oxygen vacancy improved electrochemical performance and cycling stability is mainly due to it can act as shallow donors, increasing the density of the carrier (improving conductivity) as well as improving the wettability and exposing more active sites [15,16]. Bruce Dunn reported the excellent pseudocapacitive charge storage performances of reduced α-MoO_{3-x} and pointed out the introduction of oxygen vacancies can induce larger interlayer spacing in favour of faster charge storage [4]. Up to now, various strategies have been used to enhance electrochemical performance of metal oxides by introducing oxygen vacancies (V_o), such as thermal treatment [17], chemical reduction [18, 19], and hydrogenation [8, 20]. It has been demonstrated that annealing in a reducing atmosphere is a facile, effective and reliable strategy to introduce controllable oxygen vacancy. For example, Tong [21] synthesized MnO_2 with oxygen vacancies by hydrogenation treatment. Compared with the untreated MnO_2, the electrochemical performance of the treated-MnO_2 was significantly improved with high surface capacitance up to 0.22 F cm^{-2} (449 F g^{-1}), excellent rate performance and cycle stability. Lu [22] reported hydrogenated TiO_2 nanotube arrays by annealing under hydrogen atmosphere with specific capacitance of 3.24 mF cm^{-2} (at 100 mV s^{-1}), suggested that a 40-fold increase from the reducing treatment compared to that of TiO_2 annealed in air. Sun [23] achieved improved electrochemical performance by hydrogenating a porous $NiCo_2O_4$ composite supported on Ni foam. Compared with the original material, the surface capacitance was increased from the original 0.88 F cm^{-2} to 2.1 F cm^{-2}, and the capacity retention rate was also better than that of the original material. In addition, it exhibited excellent cycle stability.

Bismuth oxy-iodide (BiOI) is one of the most promising active materials for electrochemical supercapacitors owing to its semiconducting characteristic, low cost and unique layered structure. The crystal structure is tetragonal crystal structure. It has an open layered crystal structure consisting of $[Bi_2O_2]^{2+}$ layers sandwiched between two slabs of iodide ions (Fig. 1) [24]. The typical layered structure facilitates ions diffusion and electron transport, thereby enhancing fast redox reaction kinetics. Recently,

S. Vadivel [25] reported the BiOI microsquares as electrode material, and the high specific capacitance (706 F g^{-1} at 2 A g^{-1}) can be obtained. Chen [26] prepared a BiOI material with layered structure by heating the commercial BiI$_3$ powder in air, and investigated its lithium storage properties. The experimental results show a high capacity of ~5678 mAh cm^{-2} in a potential range of 3 to 0.05V. However, the relatively poor intrinsic electronic conductivity and the small electrochemical active sites of BiOI greatly reduce its specific capacitance. As has been mentioned, introducing oxygen vacancies and constructing two-dimensional structure are an effective method to ameliorate electronic conductivity and increase electrochemical active sites.

To the best of our knowledge, introduction of oxygen vacancies and constructing two-dimensional nanosheets materials are an effective strategy to improve capacitive performance of metal oxides-based supercapacitors. Based its unique layered structure, a set of identical two-dimensional BiOI nanosheets with varied contents of oxygen vacancies were fabricated to investigate the effects of oxygen vacancies on the structure, chemistry, and electrochemical performance. Until now, there are no reports on the structure, chemistry and supercapacitor performance of two-dimensional BiOI nanosheets raised by oxygen vacancies.
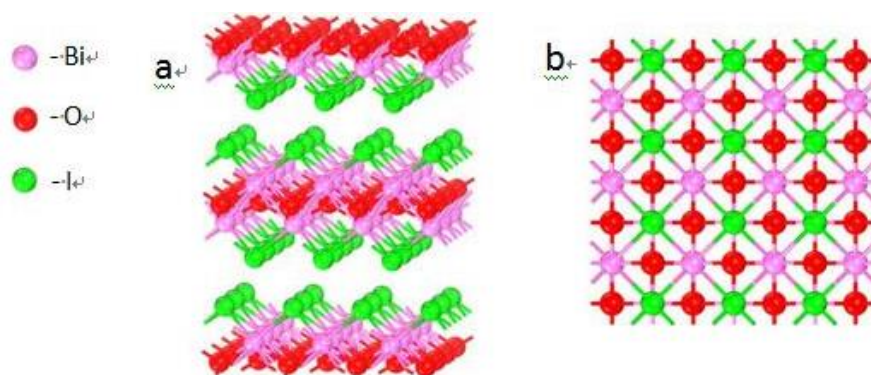

Figure 1. Schematic diagram of the crystal structure of BiOI. (a) Three-dimensional structure. (b) BiOI layer along with the [001] direction.

2. EXPERMENTAL

2.1. Material synthesis

The 2D BiOI nanosheet was obtained via a simple ions-exchange strategy at room temperature [27]. In a typical procedure, KI (0.272 g) was dissolved in 100 mL deionized water with magnetic stirring for 30 min, and was marked Solution A. Bi(NO$_3$)$_3$·5H$_2$O (0.795 g) was dissolved in 100 mL of aqueous solution with acetic acid (HAc) content (9 mL) and stirred for 30 min, and was marked Solution B. The solution B was added slowly into the solution A, and then magnetically stirred at room temperature for 1h. The suspension was aged for 4h at static condition. The resulting precipitates were collected by filtration, washed thoroughly with distilled water and ethanol, and then dried at 60 ^{o}C

overnight under vacuum to obtain the two-dimensional BiOI nanosheets. Finally, the as-prepared pristine BiOI nanosheets was annealed in a tube furnace (OTL1200 $\Phi60*1000$) at 500 ºC, 550 ºC and 600 ºC for 2 h under Ar atmosphere with a heating rate of 5ºC/min, and labeled as BiOI-500, BiOI-550, and BiOI-600, respectively.

2.2. Materials Characterizations

The crystal structures of samples were determined by X-ray diffraction using a Bruker AXS D8 advance powder diffractometer with Cu K_α radiation. The microstructure of the samples were obtained via field emission scanning electron microscopy (S-4200, Hitachi, Japan) and high-resolution transmission electron microscopy (HRTEM, JOEL, JEM-2100F). The oxygen vacancies was detected using X-ray photoelectron spectroscopy (XPS, Thermo ESCALAB 250XI with Al K_α radiation). The thermal stability of the two-dimensional BiOI nanosheets was recorded by thermal gravimetric analysis (TGA) under flowing Ar atmospheres at a heating rate of 10 ºC min^{-1} on the TA Instrument SDT Q600.

2.3. Fabrication of electrodes

The electrochemical performances of product are investigated in a conventional three-electrode configuration. A platinum sheet and an Hg/HgO electrode are applied as the counter and reference electrodes, respectively. Electrochemical measurements were performed in 6.0 M KOH aqueous solution at a potential sweep window of -1~0 V. The working electrode is fabricated by mixing the active material, acetylene black and ploytetrafluoroethylene (PTFE) in a mass ratio of 8:1:1 into a slurry and uniformly coating the single surface of nickel foam with a size of 1 cm×1 cm and dried in vacuum at 80°C for overnight.

2.4. Electrochemical Measurements

The Cyclic voltammetry (CV) and electrochemical impedance spectroscopy (EIS) measurements were performed on a CHI660E electrochemical workstation (Shanghai Chenhua, China). The CV measurement was conducted over a voltage range of -1 to 0 V at different scan rates (from 0.5 to 3 mV s^{-1}). EIS measurements were performed between 100 kHz and 0.01 Hz under an open circuit potential with an amplitude of a 5 mV. Galvanostatic charge-discharge (GCD) testing was performed on a CT-4008 neware battery testing system.

3. RESULTS AND DISCUSSION

3.1. TG-DTA analysis

The data of TG-DTA reveal phase transformation of as-prepared 2D BiOI nanosheets with the temperature from room temperature to 700 ºC at a heating rate of 5 ºC/min. As shown in Fig. 2, the TG

curve shows two major weight losses for pristine two-dimensional BiOI sample. The first stage of weight loss below 500 °C is about 1%, which can be ascribed to the dehydration of material. A major weight loss (~30.2%) in the temperature range between 500 °C and 650 °C, which can be attributed to the decomposition of two-dimensional BiOI nanosheet and formation of oxygen vacancies. A strong exothermic peak appears at 670 °C, which maybe originates from both the decomposition of two-dimensional BiOI sample and the crystallization of impurity. Above 650 °C, the weight of the sample hardly unchanged.
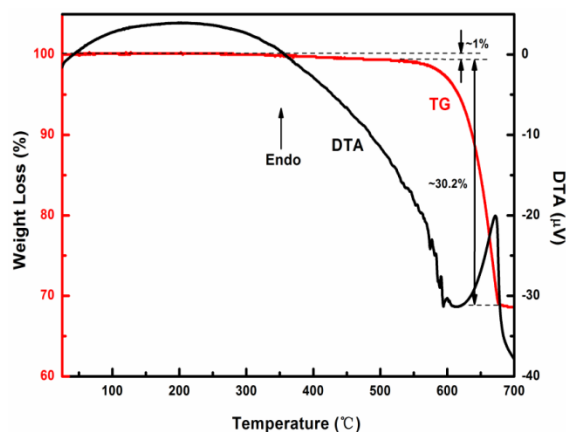

Figure 2. TG-DTA profiles of BiOI nanosheets in Ar conditions

3.2. XRD analysis

Fig. 3a shows the X-ray diffraction (XRD) profiles of the as-synthesized two-dimensional BiOI and BiOI-T samples. For fresh two-dimensional BiOI sample, the major reflections can be indexed with a *P4/nmm* space group corresponding to BiOI phase, in good agreement with JCPDS No. 73-2062. The distinct diffraction peaks at 2θ values of 9.72°, 19.46°, 29.86°, 31.61°, 37.24°, 39.38°, 45.58°, 49.97°, 51.52° and 55.39°, which are attributed to the reflections of (001), (002), (012), (110), (013), (004), (014), (005), (114) and (122) planes, respectively. No phase transformation is observed for two-dimensional BiOI-T nanosheets after reduction treatment from 500°C to 600 °C. However, a small amount of Bi_5O_7I and Bi_2O_3 are generated after reduction treatment at 650 °C for 2h. From the enlarge view of the 28-30° range (Fig.3b), there is a light shift of 2θ angle to low-angle, indicating the expansion of lattice spacing, which is mainly attributed to residual stress arising from the formed oxygen defects. The similar peak position shifts that induced by the formation of oxygen vacancy, were also observed in MoO_3 and $CoMoO_4$ nanocrystal [4, 28]. Since fresh two-dimensional BiOI sample is brownish red powder, it is surprising that the color of the reduced two-dimensional BiOI-600 nanosheets was yellow (see inset of SEM section). This is because singly charged (F^+ centers) or neutral F^0 center (color center) was formed due to the electron-trapped oxygen vacancy binding one or two electrons [29]. This also indicates that two-dimensional BiOI nanosheets was reduced.
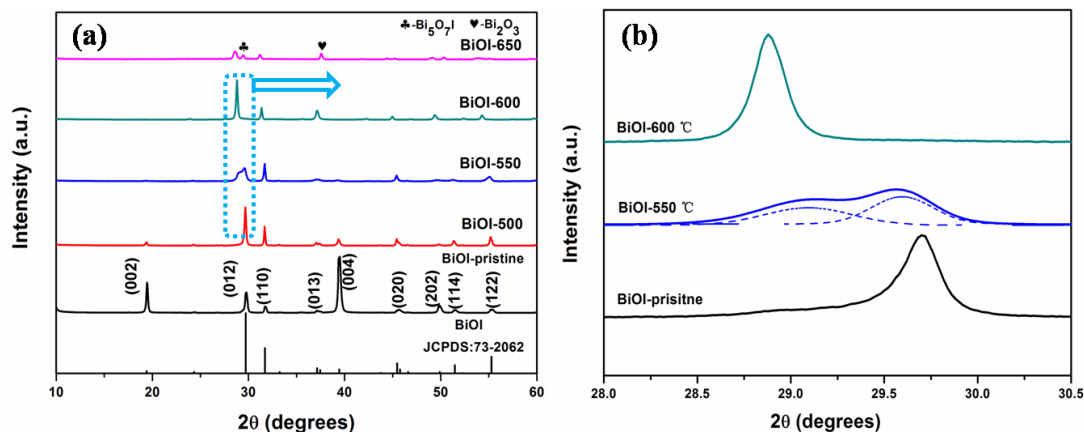
Figure 3. XRD patterns of the pristine and reduced BiOI nanosheets

3.3. XPS analysis

The change of chemical bonding environment and valence band position of fresh two-dimensional BiOI and BiOI-600 nanosheets were investigated by XPS. The O1s XPS spectra (Fig. 4) are asymmetrical and broad, indicating the existence of diverse oxygen environments. The O1s spectra can be deconvoluted into three distinct peaks centered at around 529.5 eV, 531.2 eV and 532.5 eV, which corresponding to the lattice oxygen (O_L), oxygen atoms in the vicinity of an oxygen vacancy (O_V) and chemisorbed water (O_W), respectively [30, 31].

Table 1. The percentage of different oxygen species in the decomposed O 1s.

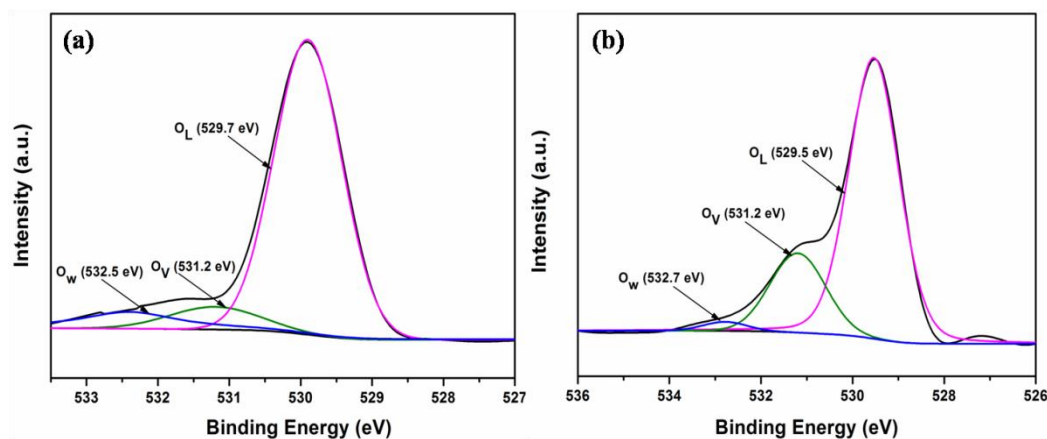| sample	O_L(%)	O_V(%)	O_w(%)
Pristine BiOI	81.67%	8.42%	9.91%
BiOI-600	75.94%	22.09%	1.97%

Figure 4. O1s XPS spectra of the pristine (a) and reduced BiOI nanosheets (b)

The calculated ratio of various oxygen species according to the fitted subpeaks area percentage is summarized in Table 1. It is clear that the O_V peak area percentage for two-dimensional BiOI-600 (22.09 %) sample is evidently larger than that in pristine BiOI (8.42 %), indicating much more oxygen vacancies on the surface during the reduction treatment, which can significantly improve the electrode material's conductivity and facilitate the surface redox reaction kinetics, and thus will enhance the capacitive performance [32, 33].

3.4. SEM and HRTEM analysis

Fig. 5 shows the SEM images of the pristine BiOI, exhibiting obvious cross-linked nanosheets characteristic and the thickness of single nanosheets is ~80 nm. As shown in Fig. 4b, comparing with the pristine BiOI, the surface of the BiOI-600 nanosheets has changed dramatically after the reduction treatment. The overall structure of the two-dimensional BiOI nanosheets was retained but the surface of the nanosheets exhibited a lot of small voids. Similarly, from the HRTEM image (Fig. 5c-d), a lot of pores with size of 2-5 nm, specified by red circles, can be observed in BiOI-600 nanosheet, which arise from the escape of oxygen and iodine gas during the thermal reduction process. The rough edges of BiOI-600 nanosheet indicated by the red lines (Fig. 5d) also signify the presence of surface defects. Further, clear lattice fringes with spacing of 0.283 nm, which correspond to the (110) plane of BiOI, can be observed in two-dimensional BiOI-600 nanosheets.
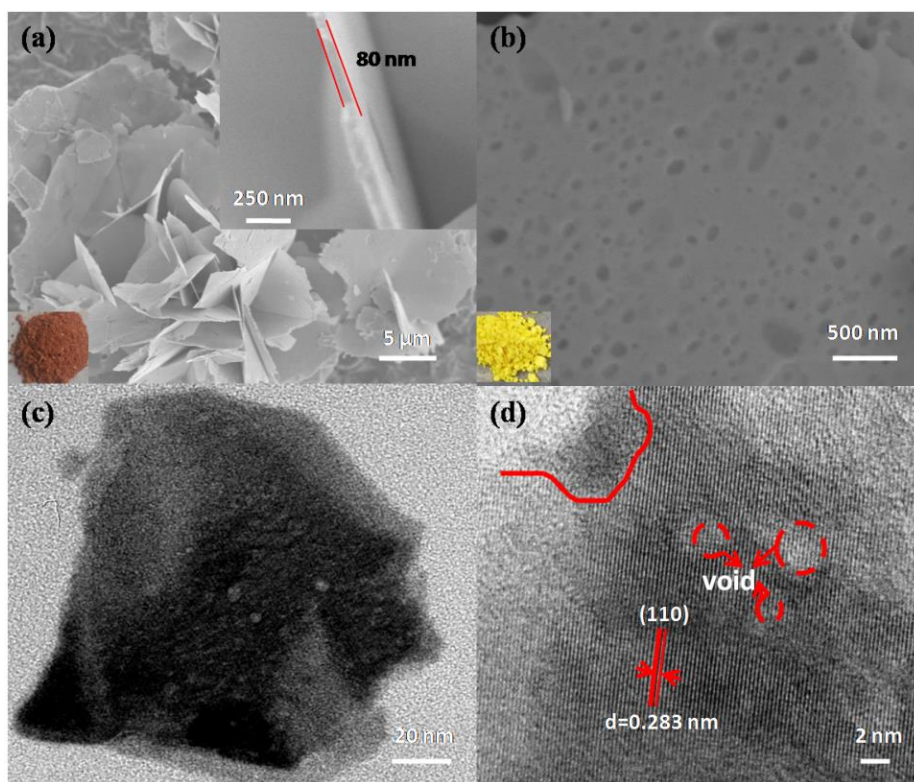

Figure 5. SEM image of pristine BiOI (a) and reduced BiOI nanosheets (b). TEM image (c) and HRTEM image (d) of the reduced BiOI nanosheets

3.5. Electrochemical analysis

It is generally believed that heat treatment in an oxygen-dificient atmosphere will induce to surface defects, which can enhance the electrical transport abilities, thus improving the electrochemical performance [34]. Fig. 6a-f shows the electrochemical properties of the two-dimensional BiOI-T nanosheet electrodes. Fig. 6a presents typical CV curves of the BiOI-T samples at the scan rate of 0.5 mV s^{-1} in a potential range of -1.0-0 V. It can be found that all electrodes show obvious oxidation and reduction peaks, suggesting that the capacitances are mainly from pseudocapacitance characteristics. Moreover, the BiOI-600 has more prominent peaks than other BiOI-T electrodes, indicating that the electrode has more rapid redox reaction rate. This is mainly due to the fact that oxygen vacancies (as revealed by the XPS analyses) on the surface of the BiOI-600 nanosheets improve the adsorption ability of OH^{-}. The GCD curves were recorded at a voltage range from -1.0 V to 0 V at 0.5 A g^{-1} to detect the influence of oxygen vacancies on the electrochemical performance (Fig. 6b). It is observed that the charge and discharge time of the BiOI-600 is bigger than those of other electrodes. The enhanced electrochemical performance of the BiOI-600 electrodes could be expounded as follows: (i) Oxygen vacancy as electron donor, can facilitate the charge transfer by introducing midgap electronic states [35]. (ii) Oxygen vancancy as active sites, can quicken the kinetics of redox reactions. The specific capacitance can be calculated according to discharge curves by using the following equation:

$$C = \frac{I \, \Delta t}{m \Delta V} \text{ (F g}^{-1})$$

Where *I* represents the discharge current (A), Δt is the discharge time (s), and ΔV represents the potential   range   of   a   discharge   (V). At the current density of 0.5 A g^{-1}, BiOI-600 nanosheets show the estimated specific capacitance of 620 F g^{-1} (Fig. 6c), while BiOI-500, BiOI-550 and pristine BiOI exhibits 330 F g^{-1}, 400 F g^{-1} and 260 F g^{-1}, respectively. The result demonstrates that the suitable oxygen vacancies can enhance the storage ability of the two-dimensional BiOI nanosheets. The redox peaks were presented in the CV curves of BiOI-600 nanosheets electrode at 0.5, 1, 2 mV s^{-1} in a potential range ranging from -1.0 to 0 V (Fig. 6d). Even if at higher scan rates, the CV curves exhibit unchangeable shapes, indicating an excellent electrochemical performance. Furthermore, a pair of nearly symmetrical redox peaks revealed good reversibility of the redox reactions of the electrode. As presented in Fig. 6e, the GCD measurements of the BiOI-600 nanosheets electrode were obtained at various current densities. The specific capacitance of the BiOI-600 nanosheets electrode is calculated to be 620 F g^{-1} at 0.5 A g^{-1}. Meanwhile, the specific capacitance at 3 A g^{-1} retains about 51% of the initial capacitance, revealing its medium rate capability. Fig. 6f shows the cycling stability of the BiOI-600 nanosheets electrode, which was measured at a current density of 1 A g^{-1}. A gradually decreasing trend was displayed, suggesting better cycling stability. After 1000 cycles, the BiOBr$_{100}$ nanosheets electrode shows specific capacitance retention of 72.5%. In addition, the as-prepared BiOI-600 nanosheets was compared with other reported bismuth oxy-based materials and the results are listed in Table 2.
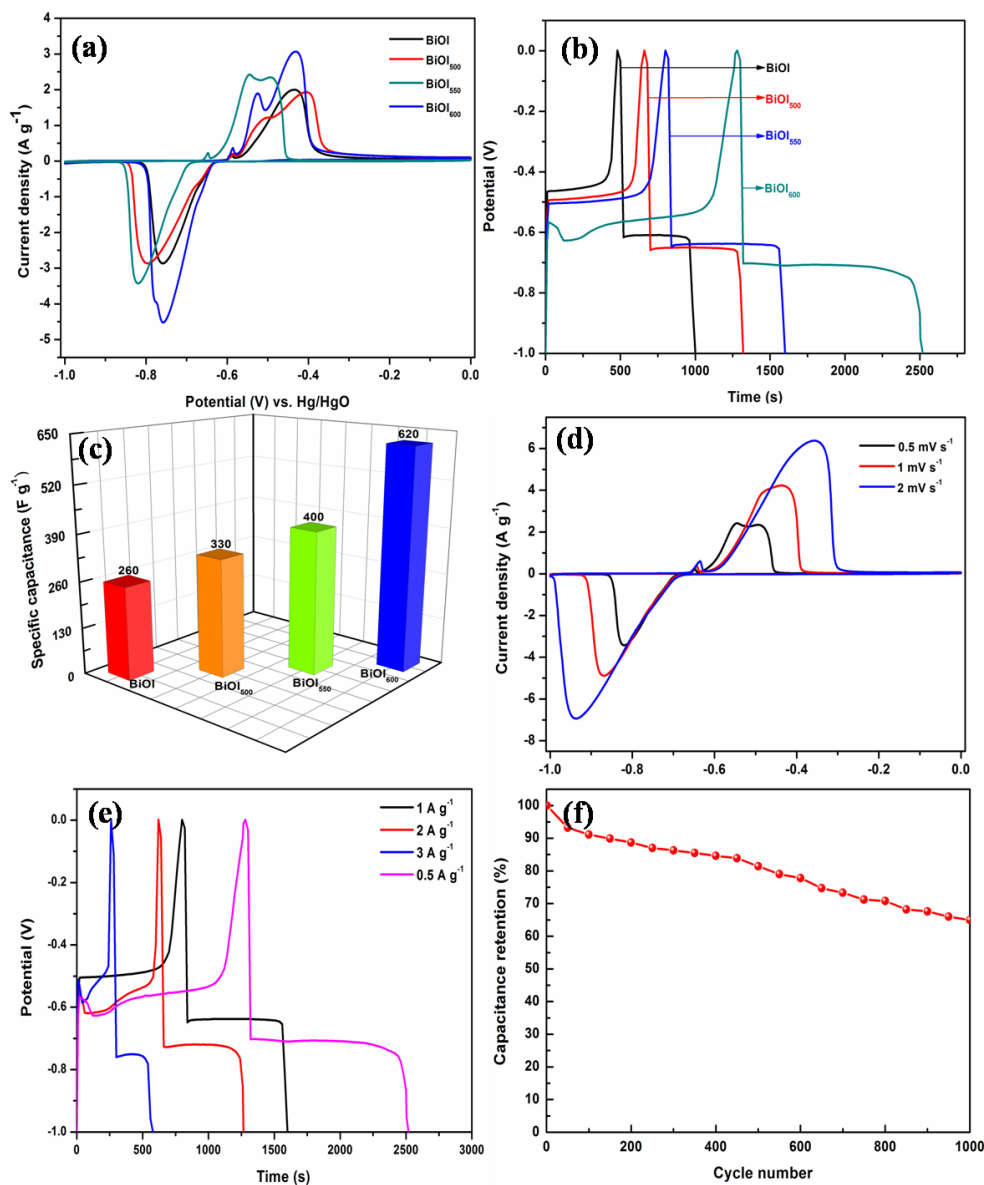
Figure 6. (a) CV curves at 0.5 mV s^{-1}, (b) GCD curves at 0.5 A g^{-1}, (c) the specific capacitance of pristine and reduced BiOI nanosheets, (d) CV curves of BiOI-600 at various scan rates, (e) GCD curves of BiOI-600 at various current density, (f) Cycling performance of BiOI-600 nanosheets at a current density of 1A g^{-1}

EIS measurements were conducted to better explain the difference in electrochemical performance among the four electrodes. The Nyquist plots of the supercapacitor electrodes of two-dimensional BiOI-T nanosheets are shown in Fig. 6. The four electrodes all show similar shape with vertical line at low frequency and semicircular nature due to Warburg resistance at high frequency region. The impedance characteristics were analyzed by the complex nonlinear least-squares fitting method on the basis of a randles equivalent circuit [41] (the inset of Fig. 7). The fitting circuits of these Nyquist plots reveal that the charge transfer resistances (R$_{ct}$) is decreased from 11.35 to 10.45 Ohm after reduction treatment of the BiOI nanosheets at 600 ^{o}C, indicating a decreased electric resistance and interface resistance due to the abundant oxygen vacancies formed on the surface of the two-dimensional BiOI nanosheets.
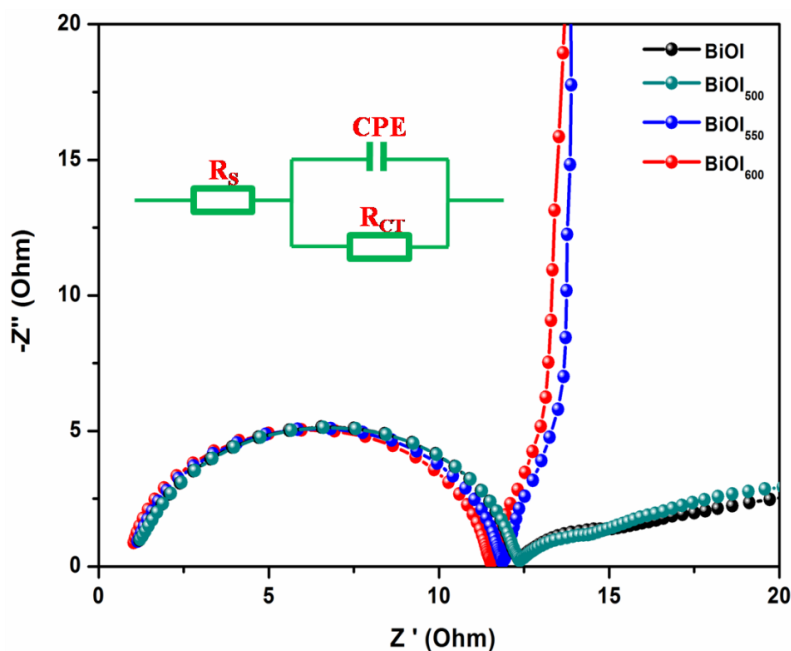
Figure 7. EIS Nyquist plots of pristine and reduced BiOI nanosheets

Table 2. Partial list of reported bismuth oxy-based materials for C_s values

Bismuth oxy-based materials	Electrolyte	C_s	Reference
BiOI microsquares	6M KOH	706 F g^{-1} (2 A g^{-1})	[25]
BiOCl nanoflake	1.0 M potassium bis(fluorosulfonyl)imide	175 mAh g^{-1} (1 A g^{-1})	[36]
BiOCl/Ti$_3$C$_2$T$_x$	1 M KOH	396.5 F cm^{-3} (1 A g^{-1})	[37]
BiOI nanosheets	1 M LiPF$_6$	717 mAh g^{-1} (30 mA g^{-1})	[38]
BiOI/Bi$_9$I$_2$	6M KOH	515.5 F g^{-1} (2 A g^{-1})	[39]
BiOI nanosheets	1 M LiPF$_6$	216 mAh g^{-1} (100 mA g-1)	[40]

4. CONCLUSIONS

In summary, a facile reduction method to produce oxygen vacancies on the two-dimensional BiOI nanosheets surface was demonstrated. The influence of oxygen vacancies on the intrinsic conductivity, microstructure, chemistry state, and supercapacitor performance was expounded. The more oxygen vacancies lead to the higher electrical conductivity as well as more electroactive site, which can dramatically enhance the pseudocapacitive charge storage properties of BiOI nanosheets. This

investigation reveals that combination of two dimensional morphology and abundant oxygen vacancies can boost the electrochemical performance of transition metal oxides.

References

1. C. R. Chen, H. L. Qin, H. P. Cong and S. H. Yu, *Adv. Mater.*, 31 (2019) 10.
2. H. C. Deng, M. W. Zhu, T. X. Jin, C. H. Cheng, J. G. Zheng and Y. Qian, *Int. J. Electrochem. Sci.*, 15 (2020) 16.
3. X. Cao, L. G. Ma, A. Q. Tian, H. L. Zhang, M. J. Zheng, S. H. Liu, Q. Li, Y. X. You, F. Z. Wang, L. Ma and W. Z. Shen, *Int. J. Electrochem. Sci.*, 15 (2020) 1160.
4. H. S. Kim, J. B. Cook, H. Lin, J. S. Ko, S. H. Tolbert, V. Ozolins and B. Dunn, *Nat. Mater.*, 16 (2017) 454.
5. K. M. Lin, K. H. Chang, C. C. Hu and Y. Y. Li, *Electrochim Acta*, 54 (2009) 4574.
6. N. Yu, H. Yin, W. Zhang, Y. Liu, Z. Y. Tang and M. Q. Zhu, *Adv. Energy Mater.*, 6 (2016) 9.
7. C. Guan, X. M. Liu, W. N. Ren, X. Li, C. W. Cheng and J. Wang, *Adv. Energy Mater.*, 7 (2017) 8.
8. X. H. Lu, G. M. Wang, T. Zhai, M. H. Yu, J. Y. Gan, Y. X. Tong and Y. Li, *Nano Lett.*, 12 (2012) 1690.
9. X. Peng, L. L. Peng, C. Z. Wu and Y. Xie, *Chem. Soc. Rev.*, 43 (2014) 3303.
10. K. Krishnamoorthy, P. Pazhamalai and S. J. Kim, *Energ. Environ. Sci.*, 11 (2018) 1595.
11. J. F. Zhang, Y. Wang, J. J. Wu, X. Shu, C. P. Yu, J. W. Cui, Y. Q. Qin, Y. Zhang, P. M. Ajayan and Y. C. Wu, *Chem. Eng. J.*, 313 (2017) 1071.
12. A. Bhirud, S. Sathaye, R. Waichal, C. J. Park and B. Kale, *J. Mater. Chem. A*, 3 (2015) 17050.
13. S. Liu, Y. Yin, D. X. Ni, K. S. Hui, M. Ma, S. Park, K. N. Hui, C. Y. Ouyang and S. C. Jun, *Energy Storage Materials*, 22 (2019) 384.
14. D. A. Tompsett, S. C. Parker and M. S. Islam, *J. Am. Chem. Soc.*, 136 (2014) 1418.
15. G. M. Wang, Y. C. Ling and Y. Li, *Nanoscale*, 4 (2012) 6682.
16. S. H. Yang, Y. Li, J. Sun and B. Q. Cao, *J. Power Sources*, 431 (2019) 220.
17. S. C. Wang, P. Chen, Y. Bai, J. H. Yun, G. Liu and L. Z. Wang, *Adv. Mater.*, 30 (2018) 7.
18. Y. Liu, B. Wei, L. L. Xu, H. Gao and M. Y. Zhang, *Chemcatchem*, 7 (2015) 4076.
19. X. Y. Kong, Y. Y. Choo, S. P. Chai, A. K. Soh and A. R. Mohamed, *Chem. Commun.*, 52 (2016) 14242.
20. L. H. Cui, Y. Wang, X. Shu, J. F. Zhang, C. P. Yu, J. W. Cui, H. M. Zheng, Y. Zhang and Y. C. Wu, *RSC Adv.*, 6 (2016) 12185.
21. T. Zhai, S. L. Xie, M. H. Yu, P. P. Fang, C. L. Liang, X. H. Lu and Y. X. Tong, *Nano Energy*, 8 (2014) 255.
22. X. Lu, G. Wang, T. Zhai, M. Yu, J. Gan, Y. Tong and Y. Li, *Nano Lett.*, 12 (2012) 1690.
23. D. S. Sun, Y. H. Li, Z. Y. Wang, X. P. Cheng, S. Jaffer and Y. F. Zhang, *J. Mater. Chem. A*, 4 (2016) 5198.
24. Y. C. Huang, H. B. Li, M. S. Balogun, W. Y. Liu, Y. X. Tong, X. H. Lu and H. B. Ji, *ACS Appl. Mater. Interfaces*, 6 (2014) 22920.
25. S. Vadivel, B. Saravanakumar, M. Kumaravel, D. Maruthamani, N. Balasubramanian, A. Manikandan, G. Ramadoss, B. Paul and S. Hariganesh, *Mater. Lett.*, 210 (2018) 109.

26. C. J. Chen, P. Hu, X. L. Hu, Y. N. Mei and Y. H. Huang, *Chem. Commun.*, 51 (2015) 2798.
27. Y. H. Lv, P. Li, Y. H. Che, C. Hu, S. L. Ran, P. P. Shi and W. Zhang, *Mater. Res.*, 21 (2018) 9.
28. K. Chi, Z. Y. Zhang, Q. Y. Lv, C. Y. Xie, J. Xiao, F. Xiao and S. Wang, *ACS Appl. Mater. Inter*faces, 9 (2017) 6044.
29. Y. H. Lv, W. Q. Yao, R. L. Zong and Y. F. Zhu, *Sci. Rep.*, 6 (2016) 19347.
30. K. Xiang, Z. C. Xu, T. T. Qu, Z. F. Tian, Y. Zhang, Y. Z. Wang, M. J. Xie, X. K. Guo, W. P. Ding and X. F. Guo, *Chem. Commun.*, 53 (2017) 12410.
31. J. Bao, X. Zhang, B. Fan, J. Zhang, M. Zhou, W. Yang, X. Hu, H. Wang, B. Pan and Y. Xie, *Angew. Chem., Int. Ed.*, 54 (2015) 7399.
32. Y. Zhao, Y. G. Xu, J. Zeng, B. Kong, X. W. Geng, D. W. Li, X. Gao, K. Liang, L. Xu, J. B. Lian, S. Q. Huang, J. X. Qiu, Y. P. Huang and H. M. Li, *RSC Adv*., 7 (2017) 55513.
33. X. F. Lu, L. F. Gu, J. W. Wang, J. X. Wu, P. Q. Liao and G. R. Li, *Adv. Mater.*, 29 (2017) 1604437.
34. G. R. Dillip, A. N. Banerjee, V. C. Anitha, B. D. P. Raju, S. W. Joo and B. K. Min, *ACS Appl. Mater. Interfaces*, 8 (2016) 5025.
35. S. H. Yang, Y. Y. Liu, Y. F. Hao, X. P. Yang, W. A. Goddard, X. L. Zhang and B. Q. Cao, *Adv. Sci.*, 5 (2018) 10.
36. W. Li, Y. Xu, Y. L. Dong, Y. H. Wu, C. L. Zhang, M. Zhou, Q. Fu, M. H. Wu and Y. Lei, *Chem. Commun.*, 55 (2019) 6507.
37. Q. X. Xia, N. M. Shinde, J. M. Yun, T. F. Zhang, R. S. Mane, S. Mathur and K. H. Kim, *Electrochim Acta*, 271 (2018) 351.
38. C. J. Chen, P. Hu, X. L. Hu, Y. N. Mei and Y. H. Huang, *Chem. Commun.*, 51 (2015) 2798.
39. S. Park, N. M. Shinde, P. V. Shinde, D. Lee, J. M. Yun and K. H. Kim, *Dalton Transactions*, 49 (2020) 774.
40. L. Q. Ye, L. J. Wang, H. Q. Xie, Y. R. Su, X. L. Jin and C. Zhang, *Energy Technology*, 3 (2015) 1115.
41. J. F. Chen, T. Zhu, X. P. Fu, G. Y. Ren and C. Y. Wang, *Int. J. Electrochem. Sci.*, 14 (2019) 7293.